Liivand, Kerli; Sainio, Jani; Wilson, Benjamin P.; Kruusenberg, Ivar; Lundström, Mari

Overlooked residue of Li-ion battery recycling waste as high-value bifunctional oxygen electrocatalyst for Zn-air batteries

Overlooked residue of Li-ion battery recycling waste as high-value bifunctional oxygen electrocatalyst for Zn-air batteries

Kerli Liivand [a,b,*], Jani Sainio [c], Benjamin P. Wilson [b], Ivar Kruusenberg [a], Mari Lundström [b]

[a] National Institute of Chemical Physics and Biophysics, Akadeemia tee 23, 12618 Tallinn, Estonia
[b] Department of Chemical and Metallurgical Engineering, School of Chemical Engineering, Aalto University, P.O. Box 16200, 00076 Aalto, Finland
[c] Department of Applied Physics, School of Science, Aalto University, P.O. Box 15100, 00076 Aalto, Finland

ABSTRACT

Continuously increasing production of Li-ion batteries (LIBs) for the Green Transition is underlined by the absence of feasible recycling methods for graphite, regardless of its criticality as a raw material. The current study demonstrates a novel strategy to valorize waste graphite as a valuable raw material in oxygen electro-catalyst production. Industrially produced LIBs post-metallurgical leach residue was transformed into highly active bifunctional oxygen electrocatalyst, which was subsequently successfully applied as an active catalyst for Zn-air batteries. Moreover, produced graphene-like material was in-situ doped by the impurity cobalt present in the recycling residue. The resultant Zn-air battery was shown to deliver a high specific capacity of 719 mA h g^{-1}, peak power density of 112.8 mW cm^{-2} and could be cycled over 400 times. Results clearly demonstrate that an often-neglected LIB recycling waste fraction can be a valuable source for electrocatalysts production required in metal-air batteries and regenerative fuel cells.

1. Introduction

Battery technology has been recognized as one of the main driving forces and key technologies required to create a carbon-neutral economy by 2050. Consequently, the battery sector is currently one of the fastest growing industries. More than 10 million electric vehicles (EVs) were on the roads in 2020 across the globe and it is anticipated that this number will rise to 125 million in 2030 and 530 million by 2040 [1,2]. Nevertheless, to obtain the full benefits of electrification the whole value chain associated with batteries needs to become more sustainable, including end-of-life recycling of spent Li-ion batteries (SLIBs) together with the ability to maximize the amounts of raw materials recovered and reused. Currently, the average lifetime of light duty EV batteries is estimated to be around 15 years, and it is predicted that already by year 2030, 0.8 million tons of EV batteries will be available for recycling [3]. In 2019 approximately < 0.2 million tons of SLIBs were globally available for recycling, of which 80% originated from portable devices [3].

Existing industrial scale SLIBs recycling processes mainly rely on pyro- and/or hydrometallurgical treatments, and have been primarily developed to efficiently recycle the most valuable battery components (Co, Ni, Cu) [4–8]. Pyrometallurgical methods apply high-temperature treatments to produce Co, Ni, Cu and Fe alloy fractions, gases, and

slag (containing Li, Mn and Al). The main disadvantages of this pathway are high energy consumption, CO_2 emissions, and that various valuable materials cannot be recovered (graphite, Al, and polymers) whereas Li recovery requires additional hydrometallurgical treatment. However, in the case of hydrometallurgical treatment, the precious cathode materials are dissolved in acids and all the main SLIBs components can be recycled. Therefore, hydrometallurgical recycling has been predicted to be the leading future recycling route for SLIBs [9]. The new recycling aims, which have been set by the European Commission in the recent Sustainable Batteries Regulation [10] include element specific targets for selected metals (Co, Ni, Cu and Li) as well as a goal for a holistic recycling efficiency (mass-%) of 70% to be achieved by 2030. Although graphite does not currently have an element specific target, it is clear that the systematic loss of this critical raw material from circulation is neither sustainable nor techno-economically desirable [11]. The necessity and criticality of addressing the issue of graphite recycling has also been recently highlighted in the road map of Batteries Europe European Technology and Innovation Platform Work Group on Raw Materials and Recycling [4]. Due to the diverse properties of graphite, it is also utilized in a variety of other industrial sectors that range from steelmaking, foundry applications, lubricants, friction materials, different energy storage systems, brushes for electrical motors to sealing applications,

fire retardants and pencils [12]. Mechanical recycling pre-treatment steps of SLIBs (e.g. via crushing and sieving) results in so called "black mass" [13–16]. This fraction is small in particle size and dominated by the active material present in cathodes (Co, Ni, Mn, Li) as well as the graphite from the anodes [17,18]. In addition, there may be various additives deriving from current collectors (Cu, Al), casing (Fe), binder (F) and electrolyte salt (F). In the case of hydrometallurgical recycling, valuable metals, and impurities (Fe, Al) dissolve into the pregnant leach solution (PLS). Also, organic chemicals and fluoride may end up to PLS if not removed during the mechanical pre-treatments. PLS is subjected to solution purification for impurity removal, after which the valuable metals are recovered. The main output waste (leach residue) of the metallurgical recycling process consists predominantly of battery-grade graphite, binder, and plastic, as well as residuals of undissolved metals. This leach residue is typically discarded as a recycling waste — by burning or landfilling (Fig. 1). Recently, various studies have addressed the topic of graphite recovery [7,19,20] including graphite separation by flotation [21,22] to be used either directly or after separation as a reductant [23,24] in high temperature (pyrometallurgical) LIB metals recycling. However, in this process the graphite is consumed as a chemical – and lost from circulation – rather than valorized as a high-value product. In contrast, several studies have investigated recycled graphite from pre-metallurgical treatment as a raw material for the preparation of graphene-like materials [25,26], which can be applied either as electrode material for batteries [27] and capacitors [28], or as a carbon support material for sensors [29] and catalysts [30]. Nevertheless, there are only a few studies [31,32] that attempt to recover and further utilize the graphite from the post-metallurgical leach residue after a hydrometallurgical battery metals recycling process. In addition, most of the published studies have been conducted with manually separated SLIB anode materials i.e., with raw material that does not represent the composition and complexity of state-of-the-art industrial SLIB "black mass" waste.

Rechargeable metal-air batteries (MABs) and regenerative fuel cells (RFCs) are considered as the next-generation electrochemical energy storage and conversion devices, however, both applications are dependent on the oxygen reduction reaction (ORR) and oxygen evolution reaction (OER), which can suffer from sluggish kinetics and high overpotentials [33–35]. Consequently, a suitable bifunctional oxygen catalyst for use in either MABs or RFCs needs to exhibit a high activity for both ORR and OER. Nonetheless, often an active ORR catalyst is not efficient for OER, and vice versa [36]. To date Pt-group metals have remained the most effective oxygen electrocatalysts, although their high cost and general scarcity of available resources makes them undesirable for widescale industrial usage. Additionally, Pt, which is still the state-of-the-art and main benchmark catalyst for ORR is inefficient for the OER, whereas the Ru benchmark catalyst for OER is conversely not sufficiently active for ORR [36]. In spite of the numerous studies on oxygen electrocatalysts [33,34,36], the development of active bifunctional catalyst with a low cost and overpotential remains challenging. Therefore, intensive study of various types transition metal nitrides [37], metal-metalloids [38], non-van der Waals 2D materials [35], and carbon materials doped with heteroatom(s) and transition metal(s) [33,34,36] have been proposed as the most promising low-cost alternatives. Various carbon-based materials—graphene, carbon nanotubes, and mesoporous carbon—are excellent catalyst supports due to their high electrical conductivity and large surface area [33,39,40]. Furthermore, the incorporation of heteroatoms, like nitrogen, into the carbon framework can modify the charge distribution and spin density of the nearby carbon atoms, and thereby increase the number of active sites available for ORR and OER [33,41,42]. It has been shown that the superior electrocatalytic ORR and OER performance originates from the synergistic effect between the nano-scale transition metal particles and N-doped carbon, represented as M-N-C (M=Co, Fe, Ni, Cu, etc.) active centers [36]. Additionally, it is known that the metal doping of a carbon structure can exhibit superior stability thanks to covalent and electronic interactions between metals and carbon [43].

In the current study, industrial black mass leach residue was used for the first time as a recycled raw material to produce a bifunctional oxygen electrocatalyst, which was subsequently utilized as an active air cathode catalyst for Zn-air batteries. The novel leach residue valorization strategy is shown schematically in Fig. 1.

2. Experimental section

2.1. Materials synthesis

Black mass leach residue from hydrometallurgical battery recycling was used as the secondary raw material and graphite source in this research. The initial black mass originated primarily from a mixture of
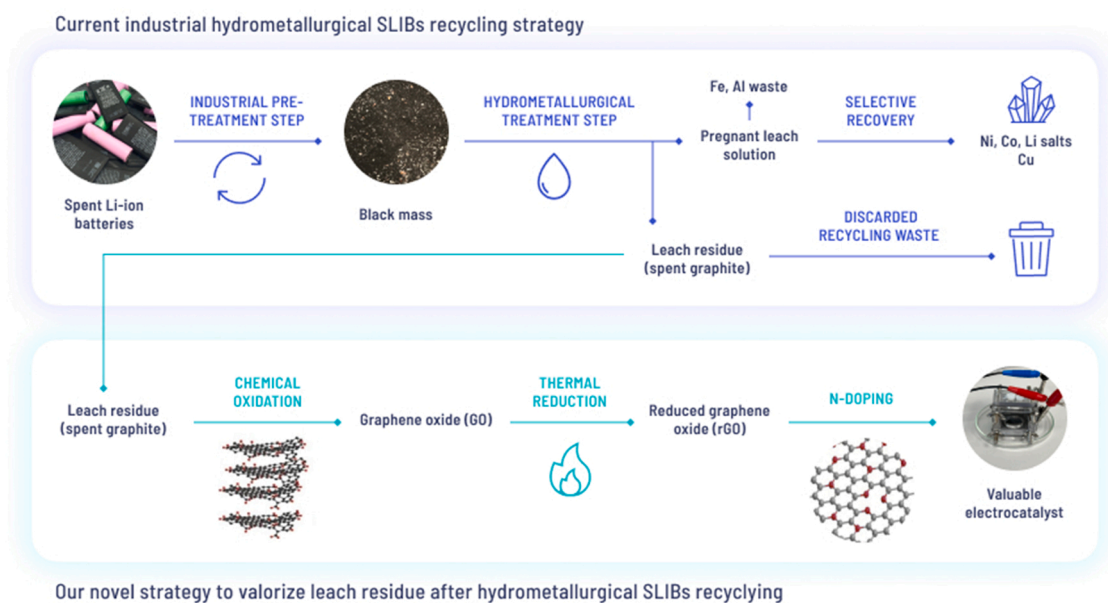

Fig. 1. Schematics of the "state-of-the-art" industrial hydrometallurgical SLIBs recycling pathway and our novel strategy for producing valuable electrocatalyst material.

portable LIBs (containing $LiCoO_2$, $LiMn_{0.5}Ni_{0.5}O_2$ and $LiMn_2O_4$ as a cathode active material), which had previously undergone industrial mechanical treatment steps - crushing, magnetic separation, and sieving process (underflow of < 500 μm fraction). This crushed and sieved black mass was subsequently treated by an efficient leaching process with 2 M H_2SO_4 at 60 °C for 3 h, with the addition of Cu and Al scrap as reductants - a procedure described in more detail in Chernyaev et al. [18]. The graphite contained within the SLIB leaching residue was used as a raw material for Bat-GO synthesis by a modified Hummers procedure [44,45]. Initially, 2.0 g of SLIB leached residue was mixed with 50 ml of H_2SO_4 (95%, VWR, USA) and sonicated for 1 h. Thereafter, the mixture was placed into an ice bath on a magnetic stirrer, to keep the mixture temperature low, and 2.0 g of $NaNO_3$ (>99.5%, Merck, Germany) was added. This was followed by the addition of 6.0 g of $KMnO_4$ (>98%, IS-VET OY, Finland) in very small portions, over a time-period of 45 min, to have better control over the exothermic reaction. Once all $KMnO_4$ was added, the mixture was heated to 35 °C and the temperature maintained for a duration of 18 h. Finally, the mixture was placed into an ice bath and 80 ml of deionized H_2O and 20 ml of 30% H_2O_2 (VWR, USA) were added. After the chemical oxidation step, the synthesized Bat-GO mixture was centrifuged, firstly 3 times with a 10% HCl (VWR, USA) solution to remove dissolved metals and, subsequently, with de-ionized water until an almost neutral pH of the supernatant was achieved. Finally, the obtained material was dried in an oven at 60 °C for at least 48 h. Analysis of the yield showed that from 2.0 g of SLIB leached residue 1.8 g of Bat-GO was synthesized.

The Bat-N-rGO electrocatalyst was prepared by a two-stage pyrolysis process. In the first step, the Bat-GO was thermally reduced to Bat-rGO in a tube furnace (Nabertherm, Germany), at 800 °C for 1 h under an Ar gas flow. During this process most of the oxygen functional groups were removed and 0.35 g of Bat-rGO was produced from 1.0 g of Bat-GO, respectively. Finally, electrocatalytically active electrocatalyst Bat-N-rGO was synthesized by nitrogen doping of the Bat-rGO sample with the second pyrolysis step. Dicyandiamide (DCDA, Sigma-Aldrich, Germany) was used as a nitrogen source and polyvinyl pyrrolidone (PVP, Sigma-Aldrich, Germany) was added as a dispersing agent. A Bat-rGO/DCDA/PVP mixture, with mass ratios of 10/200/1, was sonicated for 2 h in ethanol solution. Thereafter, the ethanol was evaporated, and the mixture was pyrolyzed at 800 °C for 2 h under an Ar gas flow - from 0.100 g of Bat-rGO 0.098 g of Bat-N-rGO catalyst was produced.

2.2. Materials characterization

The surface morphology and bulk phase composition of materials were achieved with scanning electron microscopy (SEM) Mira 3 (Tescan, Czech Republic) equipped with an UltraDry Silicon Drift energy-dispersive X-ray spectrometer and NSS microanalysis software (EDS, Thermo Fisher Scientific, USA) or with ZEISS FE-SEM Ultra 55 (Carl Zeiss Microscopy, Germany). The crystallinity of the materials was studied with the X-ray powder diffraction (XRD) (X´Pert3, PANalytical, The Netherlands) and XRD diffractograms were obtained with Cu Kα radiation ($\lambda = 1.54182$ Å), measured with a step size of 0.026 at 45 kV and 40 A. High ScorePlus software was applied to analyze and fit the obtained spectrums. The metal content (mg/g) in the SLIB leach residue and Bat-rGO sample were determined by the total leaching of material in aqua regia to produce a solution from which the metal content was analyzed by flame atomic adsorption spectroscopy (AAS, Thermo Fisher, ICE 3000, USA). To gain more information about the structural properties of carbonous samples Raman spectroscopy was used. Raman spectra were recorded with Confocal Raman microscope (Renishaw inVia™, UK) using a 532 nm wavelength laser beam and data fitting was undertaken with OriginPro (OriginLab Corporation, USA) using an applied Voigt function. HRTEM images were taken with a JEOL JEM-2200FS double aberration-corrected microscope equipped with a 200 kV field-emission gun and X-ray EDS detector (JEOL Ltd., Japan). X-ray photoelectron spectroscopy (XPS) was carried out with a Kratos Axis

Ultra spectrometer (Kratos Analytical Ltd, UK) with monochromated Al Kα-radiation and charge neutralization, a pass energy of 40 eV and X-ray power of 195 W. The analysis area comprised of an area approximately 700 μm x 300 μm and the sp2 carbon 1 s peak at 284.6 eV was used as a charge reference point. Elemental composition of the samples was determined from the high-resolution core level spectra peak areas after Shirley background subtraction using equipment specific sensitivity factors. Peak fitting was done using Gaussian-Lorentzian peaks (GL (30) line shape in CasaXPS) with the peak positions fixed to within ± 0.1 eV of the given binding energies. For the N 1 s region, the full width at half-maximum (FWHM) of the peaks was restricted such that they were equal. In contrast, the broader N-oxide peak was restricted to positions between 403 and 405 eV with the FWHM restricted to below 4 eV. To determine the specific surface area and pore size distribution of Bat-rGO and Bat-N-rGO samples, N_2-adsorption/desorption isotherms were measured using a NOVAtouch LX gas sorption analyzer (Quantachrome, USA). The results were analyzed by Brunauer-Emmett-Teller (BET) and density functional theory (DFT) methods in order to calculate the specific surface areas and pore size distribution, respectively.

2.3. Electrochemical measurements

To study the electrocatalytic activity of Bat-N-rGO electrocatalyst RDE, RRDE and chronoamperometric methods were used, and commercial 19.8% Pt/C (Tanaka Kikinzoku Kogyo K.K., Japan) and RuO_2 (99.9% Alfa Aesar, USA) catalysts were measured for comparison. A three-electrode cell setup was used to investigate the performance of electrocatalysts towards oxygen reduction reaction (ORR) and oxygen evolution reaction (OER) in 0.1 M KOH electrolyte. For RDE and chronoamperometry measurements, glassy carbon (GC) encased into a Teflon shell to provide a geometric area of 0.2 cm^2 was utilized as the working electrode, whereas the RRDE measurements made use of a Pt ring with GC disk (0.23 cm^2) surrounded by a PEEK shroud. The counter electrode was either a graphite rod (for the RDE and chronoamperometry) or Pt wire (RRDE) and an Ag/AgCl electrode combined with a salt bridge was used as a reference electrode in all cases. All potentials were measured vs. Ag/AgCl, however to aid comparison, all potentials have been re-calculated to vs. a reversible hydrogen electrode (RHE), which based on the calibration of the Ag/AgCl electrode vs. RHE $= -0.964$ V. RDE was carried out with a Gamry potentiostat/galvanostat Interface 1010E (Gamry Instruments Inc., USA), equipped with an Origalys speed control unit, while for RRDE measurements with MSR Rotator (Pine Research, USA) and CompactStat.h (bi-)potentiostat (Ivium Technologies BV, The Netherlands). Prior to each measurement, the GC surface was polished to a mirror finish with 1 and 0.2 μm alumina slurries. For the study of the Bat-N-rGO and Bat-rGO material electrocatalytic properties towards ORR and OER, catalyst suspensions in ethanol (4 $mg_{catalyst}$/ml) with 24 μl of aQPS-s14 ionomer (2%, Hephas Energy, Taiwan) were prepared. Suspensions were sonicated for 40 min prior to the GC modification and the final catalyst loading on the electrode was 400 μg/cm^2. For comparison, commercial 19.8% Pt/C catalyst (Tanaka Kikinzoku Kogyo K.K., Japan) for ORR and 99.9% RuO_2 (Alfa Aesar, USA) for OER were used, suspensions of 1 $mg_{catalyst}$/ml in isopropanol and water mixture with addition of 1μl of aQPS-s14 ionomer was prepared, resulting in a final loading of 19.8 μg cm^{-2} of Pt and 80 μg cm^{-2} of RuO_2 on the GC surface. All electrochemical experiments were carried out at room temperature (22 ± 1 °C) in 0.1 M KOH solution. Before carrying out the electrochemical measurements the electrolyte was saturated with O_2 (ORR) or N_2 (OER) gas and the gas flow was maintained over the electrolyte for the duration of the experiments. All linear sweep voltammetry (LSV) curves were recorded at a scan rate of 2.5 mV s^{-1}. ORR and OER polarization curves were iR-compensated after the experiment by through iR-drop elimination with respect to the ohmic resistance of the solution as determined from EIS data (38 ± 1 Ω). These resistance values were ascertained from the EIS measurements within the frequency region from 100 kHz to 1 Hz (with 10 mV

modulation) at the open circuit potential. The resistance value is found from Nyquist plot, from the real part impedance when the imaginary part of the impedance is zero. In order to study the catalyst materials long term stability and methanol tolerance, chronoamperometry measurements were performed at 0.76 V vs. RHE in O_2 saturated electrolyte. For chronoamperometry the RDE rotation was fixed at 200 rpm, whereas for the methanol tolerance investigation the speed was increased to 1600 rpm and methanol was added after 300 s to result in a 3 M MeOH solution.

RRDE measurements were performed with Bat-N-rGO catalyst to directly obtain the selectivity of H_2O and/or H_2O_2 formation during the oxygen reduction process in O_2 saturated 0.1 M KOH electrolyte at rotation speed 1600 rpm with a potential of 1.2 V applied to the outer Pt ring to detect the peroxide. The percentage of H_2O_2 produced and the number of electrons transferred during ORR were calculated based on the following equations:

$$H_2O_2\% = 100 * \frac{2I_r/N}{I_d + I_r/N} \tag{1}$$

$$n = \frac{4I_d}{I_d + I_r/N} \tag{2}$$

where I_d is the disk current, I_r is the ring current and N is the RRDE collection efficiency (0.383, provided by the manufacturer).

For Tafel slopes, ORR and OER polarization curves measured at 1600 rpm were used with the kinetic-limiting current density (j_k) calculated based on the following:

$$j_k = \frac{j \times j_d}{j - j_d} \tag{3}$$

where j is the current density and j_d diffusion-limiting current density.

To demonstrate a practical application of the Bat-N-rGO catalyst, an in-house rechargeable Zn-air battery (ZAB) was fabricated. The ZAB air cathode was prepared by drop-casting the catalyst (with a loading of 1.0 mg cm^{-2}) onto a commercial gas diffusion layer (GDL, SGL DC-28). 4 mg Bat-N-rGO electrocatalyst and 8 µl Nafion ionomer solution (5%, Sigma- Aldrich) was dispersed in 0.658 ml ethanol and sonicated for 30 min. ZAB was assembled with a polished Zn plate (1 mm, 99.9%) as the anode, 10 ml of 6 M KOH as the electrolyte and prepared air cathode (with an exposed active area of 0.79 cm^{-2}) with a Ti mesh (current collector). For comparison, a ZAB with an air cathode containing commercial catalyst was prepared, mixture of 19.8% Pt/C and RuO_2 (99.9%) catalyst (Pt/C+RuO_2), with a mass ratio of 1:1 and final catalyst loading of 1.0 mg cm^{-2} on GDL. ZABs testing was performed at room temperature under ambient atmosphere with an Autolab potentiostat/ galvanostat. Current and power densities were normalized to the effective surface area (0.79 cm^2) of the air electrode and the specific capacity was calculated based on the mass of consumed Zn metal. The cycling performance was assessed by employing galvanostatic 5 min discharging and 5 min charging at a current density of 5 mA cm^{-2}.

3. Results and discussion

3.1. Raw material

The black mass leached residue used as raw material for electrocatalyst preparation originated from industrially crushed SLIB fine fraction [46], which was previously subjected to a hydrometallurgical recycling [18]. Analysis of the SLIB leach residue (Fig. 2) shows that it consisted mainly of graphite, some unleached cathode materials (Co, Li, Ni, Mn) and other solids like binder (F source), Al, Cu, Fe and Si, as shown by the related XRD (Fig. 2b), elemental SEM-EDS (Supplementary Information, Fig. S1) and AAS analysis (Table S1). The crystalline phases identified in the residue by XRD analysis comprised primarily of graphite (ICDD: 96–900–8570), $Li_{0.61}CoO_2$ (ICDD: 98–018–2347), Li_2MnO_3 (ICDD: 98–007–3370), LiO_2 (ICDD: 98–018–0561) and Ni_4 (ICDD: 96–901–3034) and is typical of industrial black mass leach residue. During the characterization it was also found that the material was heterogenous in nature - due to the mixture of different battery fractions within the original industrial black mass - as previously reported by others [47,48].

3.2. Chemical oxidation and reduction of SLIB leach residue – behavior of graphite

With the chemical oxidation (modified Hummer's method) the graphite in SLIB black mass leach residue was completely transformed into graphene oxide (Bat-GO) and thereafter, by thermal treatment, into reduced graphene oxide (Bat-rGO, Fig. S2). The XRD spectra (Fig. 3a) reveals that the chemical oxidation of graphite was successful as the main characteristic graphite (002) peak at 26.7°, is completely absent from the Bat-GO spectra, and the characteristic GO (001) peak at 10.3° is evident. This demonstrates that the D-spacing between the graphite lattices has increased from 3.34 Å to 8.59 Å, confirming that the graphite is completely oxidized and exfoliated [30]. After thermal reduction of the Bat-GO (Bat-rGO) sample and Bat-rGO (Bat-N-rGO) nitrogen doping, the XRD spectra has two broad peaks, (002) and (001) peak. The re-emergence of the (002) peak demonstrates that the bulky
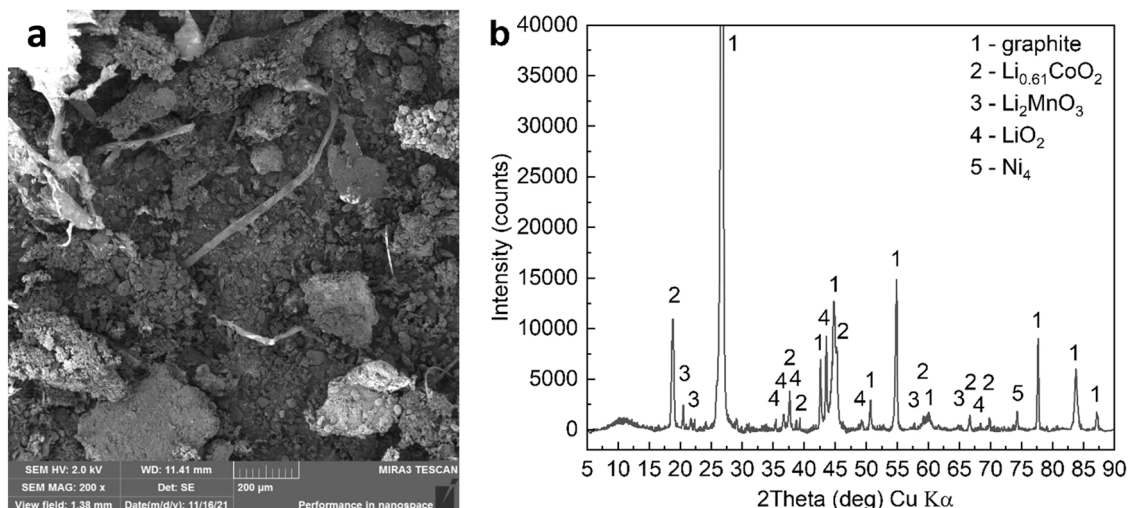

Fig. 2. a) SEM image and b) XRD diffractogram of raw material used (SLIB leach residue).
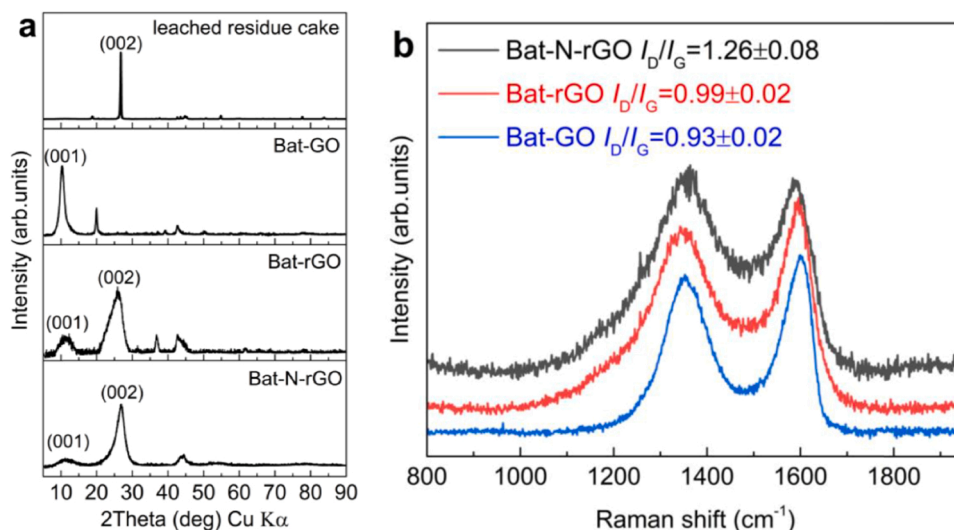
Fig. 3. a) XRD diffractograms of the SLIB leach residue, Bat-GO, Bat-rGO and Bat-N-rGO samples, b) Raman spectra of Bat-GO, Bat-rGO and Bat-N-rGO samples.

oxygen groups have been removed from the carbon basal plane and that the graphene layers have started to repack together, although the increased peak width is indicative of a highly amorphous phase content. In addition, the still existent (001) peak shows that not all the oxygen groups have been completely reduced with the thermal treatment. XRD diffractogram trends for Bat-rGO and Bat-N-rGO samples are relatively similar, however, closer examination shows that the (002) peak maximum has shifted from 25.90° to 26.97° - corresponding to a D-spacing change from 3.44 nm to 3.30 nm - due to the nitrogen and metal doping. This demonstrates that the nitrogen and metal functionalities have been embedded into the carbon lattice resulting in higher structural refinement, which is also supported by the decrease in the (002) peak width in the case of Bat-N-rGO sample. From literature it is known that doping with Co nanoparticles can improve the graphitization of the supporting carbon material [49].

3.3. Chemical oxidation and reduction of SLIB leach residue – behavior of metals

It was found that chemical oxidation of SLIB leach residue in concentrated sulfuric acid by sodium nitrate and potassium permanganate not only results in the oxidation of graphite, but also dissolution of residual metals in the material (Table S2). AAS analysis was performed to determine the bulk content of metals in the Bat-rGO sample following the chemical oxidation.

and reduction by heat treatment (Table S3). A clear majority of the metals were shown to be dissolved during the chemical oxidation step and subsequently removed from the Bat-GO mixture with the supernatant phase (10% HCl) during the first centrifugation (Table S2).

After a further two rounds of centrifugation with 10% HCl, only traces of metals could be found in the supernatant solution and these removed metals can consequently be recovered back to circulation by state-of-the art methods [50,51]. The Bat-GO mixture was then subjected to additional centrifuge treatment in the presence of de-ionized water in order to achieve a more neutral pH. XRD analysis revealed that the finally collected Bat-GO sample also contained Co, peaks visible at 19.9°, 39.1°, 42,6° and 50.2°, corresponding to Co (ICDD:94–410–5681) (Fig. 3a). In the case of Mn, Fe, Ni and Li, only traces (< 0.34 mg/g) were detected in the Bat-rGO sample, whereas Co – which had the highest content in the SLIB leach residue – clearly remained (17.7 mg/g). The presence of Co in the Bat-rGO sample was similarly confirmed by SEM-EDS (Fig. S3), the results of which also showed that Co content was highest (~ 1.9%) cf. the other metals (< 0.43%). Further SEM-EDS mapping also detected the existence of Si in

the original leach residue (Fig. S1), as well as in the Bat-rGO (Fig. S3) and Bat-N-rGO (Fig. S4) samples. These findings indicate that the original SLIBs have contained some fraction of Si or SiO_2 within the anodes, which is used in batteries to increase the cell energy [8]. Nevertheless, due to the inert nature of silicon-based materials neither the chemical oxidation nor thermal treatment influenced the content of Si. After the second heat treatment and nitrogen doping, the Bat-N-rGO sample SEM-EDS analysis showed the presence of Co and Si as the only remaining components (in addition to graphite) that arise from the SLIB composition (Fig. S4 and S5). This clearly demonstrates that chemical oxidation followed by thermal reduction treatment is sufficient to remove the majority of the SLIB components (except for some Co and Si) present in the graphite rich black mass leach residue and no additional treatment/purification steps are needed.

3.4. Physicochemical characterization of Bat-rGO and Bat-N-rGO samples

To further investigate the changes in the carbon structure, Raman spectroscopy characterization was performed. Presence of the D band at ~ 1350 cm^{-1}, G band below ~ 1600 cm^{-1} and the broad overlapping peaks displayed in Fig. 3b are typical for GO and related species [30]. In addition, as the I_D/I_G intensity ratio reflects the disorder degree in carbonous material structure, this ratio increases with every additional synthesis step - from 0.93 ± 0.02–0.99 ± 0.02, and finally to 1.26 ± 0.08 – further demonstrating the extent of the carbon lattice disruption due to thermal reduction and the embedding of nitrogen and metal functionalities into the carbon framework. It has been shown that defect-rich carbon material, with defective edges and pores, exhibits higher catalytical activities than defect-free carbon [36,43]. These defects on carbon lattices can provide the required anchoring sites for metals and nitrogen, to form multi-active M-N-C centers, which can lead to superior ORR and OER performance and stability [36,43]. The elemental composition and surface morphology of Bat-rGO and Bat-N-rGO samples were also investigated by TEM-EDS (Fig. 4a-4b, S6-S8). Characterization of Bat-rGO (Fig. 4a) and Bat-N-rGO (Fig. 4b) samples by HRTEM display the presence of graphene sheets with a flowing transparent structure and wrinkles. An additional HRTEM image (Fig. S6) of the Bat-rGO sample shows that a graphene-like material - that consists of few- and multilayer graphene sheets - was successfully obtained from the SLIB leached residue graphite by chemical oxidation and thermal reduction. In the case of the Bat-rGO sample, unevenly distributed metal particle agglomerates with sizes from 50 to 200 nm - comprised of Co and Fe (Fig. S7) - were observed between the
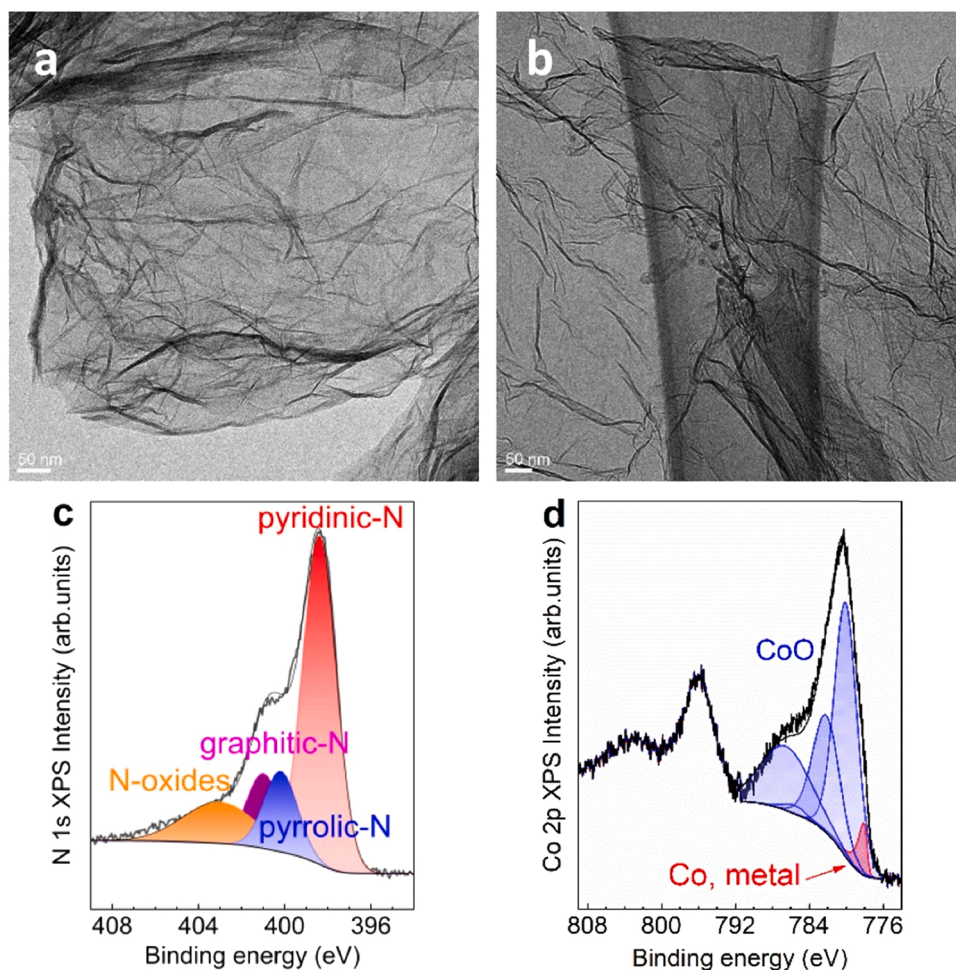
Fig. 4. HRTEM image of a) Bat-rGO and b) Bat-N-rGO samples. XPS of the Bat-N-rGO sample: c) N 1 s region and d) Co 2p region.

graphene sheets. Such agglomerates are remnants of the active cathode material residue that originates from the initial black mass, and it was determined that the presence of these metal agglomerates can catalyze the growth/formation of bamboo-structured carbon nanotubes (Fig. 4b and S8) during the nitrogen doping process. Bamboo-structured carbon nanotubes are made up of hollow carbon compartments that have grown along the same axis and are connected to each other by knots [52]. Based on literature, it is known that these types of CNT have high surface area and density of defects and are often formed during the pyrolysis when cobalt or iron nanoparticles are present with a nitrogen source [53,54]. After growth/formation of the bamboo-structured carbon nanotubes has taken place, it is evident that the metal particles were no longer agglomerated and were somewhat more evenly distributed across the graphene sheets, with the Co particles in particular appearing to be encapsulated within these freshly grown bamboo-structured carbon nanotubes (Fig. S8). The encapsulated Co is protected by the carbon layer, which prevents corrosion and oxidation [49]. Furthermore, these unevenly distributed bamboo-structured carbon nanotubes may have beneficial properties as spacers between the graphene layers, preventing the van der Waals forces-driven restacking of the graphene sheets, leading to an increase in the surface area and, thereby, the mass and ion transfer kinetics. The restacking of graphene layers leads to both a reduction in the active surface area and a decrease in the number of electrocatalytically active sites, therefore, carbon nanotubes are often required to be added separately to the graphene-like catalysts to ensure suitable levels of activity [42,45]. The chemical composition of the Bat-N-rGO catalyst surface was studied using XPS (for comparison to Bat-rGO, see Supporting Information). Figs. 4c-4d show the N 1 s and Co

2p regions of the Bat-N-rGO sample and their relative contents were 9.8 and 1.0 at%, respectively. O 1 s, C 1 s and survey spectra as well as the related atomic concentrations are provided in Fig. S9 and Table S4. Fig. 4c shows the N 1 s spectra for the Bat-N-rGO sample, which has been fitted using four types of N-functional groups as the basis: pyridinic-N (ca. 398.3 eV), pyrrolic-N (ca. 400.1 eV), graphitic-N (ca. 400.9 eV) and N-oxides (ca. 403 eV) [55]. From the results, it is clear that a majority of the nitrogen is in pyridinic form (57%), with roughly equal amounts of the other functional groups, suggesting that the presence of Co atoms can increase the content of pyridinic-N. Although the type of nitrogen species that plays the major role for ORR and OER is still open to debate, numerous studies have indicated that the presence of pyridinic-N and graphitic-N (quaternary-N) species can be considered as the most beneficial [36,41,45,49,56]. Additionally, pyridinic-N can provide more stable anchoring sites for single metal atoms within the carbon structure and pass on the positive charge to the neighboring sp^2 carbon atoms by supporting reactant adsorption and boost charge transfer among reaction intermediates and active surface, consequently leading to an increase in ORR and OER kinetics [43,57].

Also, Zhang et. al. demonstrated that the strong coupling between of cobalt oxide, nitrogen and rGO can play a crucial role in the enhancement of the catalytic activity for ORR and OER [58]. Peak fitting results are summarized in Table S4. Fig. 4d shows the Co 2p spectra of the B-N-rGO sample that features a 2p$_{3/2}$ peak at ca. 780.4 eV and a corresponding broad satellite peak at ~787 eV, which is typical for Co(II) [59]. Subsequent fitting of the 2p$_{3/2}$ peak with two peak envelopes corresponding to metallic Co and CoO required only a minor metallic component (9%) signifying that a majority of cobalt was present as CoO

[59]. This can be beneficial, as it has been shown that a combination of cobalt oxide and carbon materials can improve catalytic performance [49]. Nevertheless, other Co(II) compounds cannot be excluded either, since the fit is not very sensitive to the exact compound type. N_2-adsorption/desorption analysis were performed to gain additional information about the textural characteristics of Bat-rGO and Bat-N-rGO sample (isotherms shown in Fig. S10a). Typically, battery grade graphite usually has a low specific surface area between 2 and 6 m^2 g^{-1} [60], following treatment to breakdown the refined graphite structure of the SLIB to Bat-rGO, the specific surface area was increased to 302.9 m^2 g^{-1}, although subsequent incorporation of nitrogen species into the graphene-like structure (Bat-N-rGO) resulted in a reduction of the measured surface area to 243.5 m^2 g^{-1}. Nevertheless, determination of the related pore sizes demonstrated that there were only minor changes to the distribution following nitrogen doping (Fig. S10b).

3.5. Bat-N-rGO electrocatalytic activity towards of ORR and OER

The electrocatalytic activity of Bat-N-rGO catalyst towards of ORR was shown to be exceptionally high as the onset potential (E_{onset}) of 0.964 V is only 0.021 V lower than that of the commercial 19.8% Pt/C benchmark catalyst (Fig. 5a). Moreover, the half-wave potentials ($E_{1/2}$) were also determined to be of a similar magnitude with $E_{1/2}$ = 0.849 V for Bat- N-rGO and 0.863 V for 19.8% Pt/C catalyst, respectively. In contrast, a very high diffusion limiting current density value of − 7.34 mA cm^{-1} at 1600 rpm was measured for the Bat-N-rGO catalyst, a value which is significantly higher than that achieved for the 19.8% Pt/C

catalyst under the same conditions (Fig. 5a and S11a). From the Bat-N-rGO cyclic voltammetry curves the presence of the Co(II)/Co(III) redox pair was visible (Fig. S11b), which was to be expected based on the results with XPS, TEM-EDX and XRD. Further investigations with the Bat-rGO sample also demonstrated that a relatively high catalytic activity could also be achieved— cf. 19.8% Pt/C catalyst (Fig. 5a)—even prior to the doping with nitrogen: E_{onset} = 0.870 V and diffusion limiting current density of − 5.33 mA cm^{-2} at 1600 rpm (Fig. S11c). However, the superior performance of Bat-N-rGO, with higher onset potential and limiting current density, highlights the critical role of Co-N-C active sites on ORR catalytic activity. In addition to the superior ORR activity, the Bat-N-rGO catalyst also displayed advantageous OER activity (Fig. 5b) with a level of overpotential similar to that of a commercially available benchmark RuO_2 catalyst. The OER overpotential values for Bat-rGO, Bat-N-rGO and RuO_2 at a current density of 10 mA cm^{-2} were 0.509, 0.436 V and 0.405 V, respectively (Fig. 5b). All ORR and OER polarization curves were iR-compensated with respect to the ohmic resistance of the solution as determined from EIS data (38 ± 1 Ω, Fig. S12). It has been showed, that the N-Co co-doping of carbon can reduce the OER barrier [49]. Moreover, Chang et al. showed that uniformly distributed cobalt oxide enhanced the OER by demonstrating strong oxidability and could chemically absorb and oxidize various OER reaction spices [61]. However, the nitrogen doping of Bat-rGO noticeably increases the activity for oxygen evolution catalysis, demonstrating that the nitrogen functionality with cobalt species also play a crucial role to catalyze the oxygen evolution reaction. From these results it is evident that the Bat-N-rGO catalyst shows high electrocatalytic activity towards both,
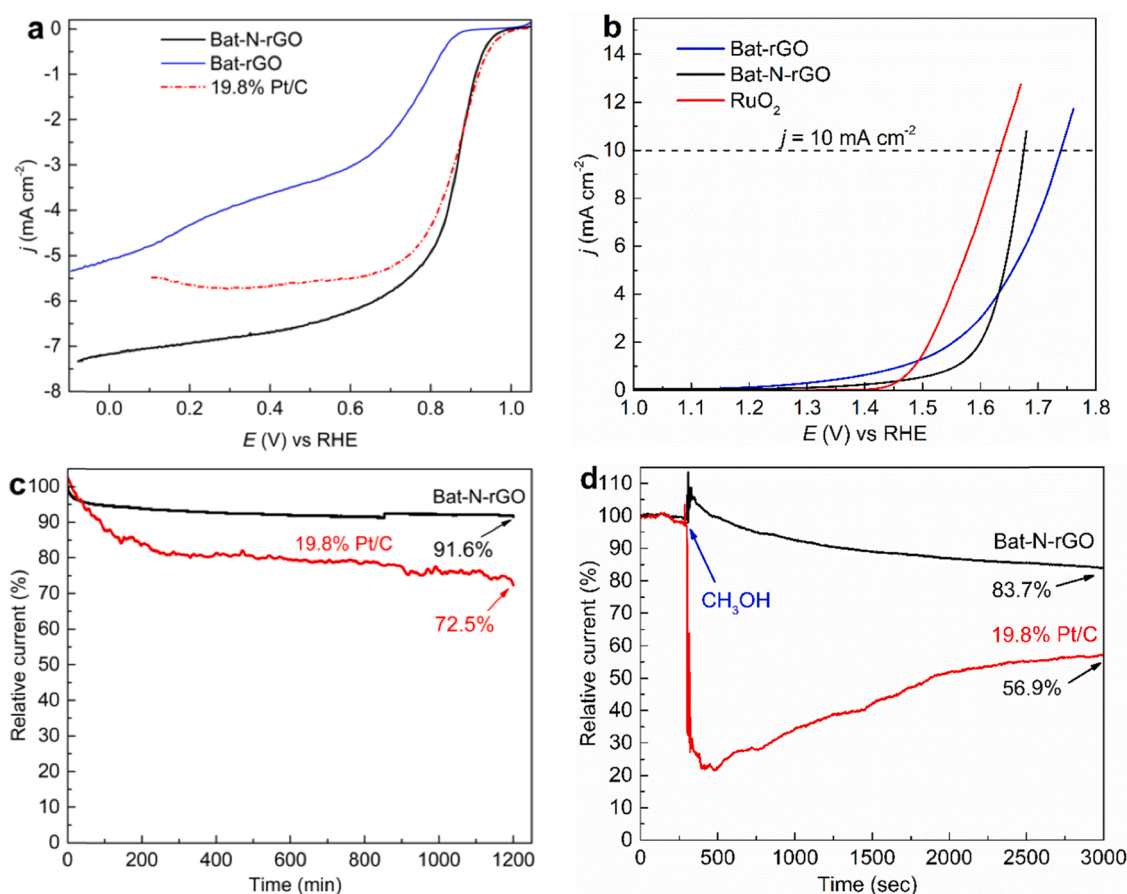

Fig. 5. a) Comparison of Linear Sweep Voltammetry (LSV) oxygen reduction results with different catalysts (Bat-rGO, Bat-N-rGO and 19.8% Pt/C) on modified Glassy Carbon (GC) electrodes in O_2 saturated 0.1 M KOH solution, v = 2.5 mVs^{-1} at 1600 rpm. b) RDE LSV curves for oxygen evolution on GC modified with Bat-N-rGO and RuO_2 catalysts in N_2 saturated 0.1 M KOH solution, v = 2.5 mVs^{-1} at 1600 rpm. c) Chronoamperometric response obtained for Bat-N-rGO and 19.8% Pt/C catalysts at 0.764 V at rotation speed of 200 rpm in O_2 saturated 0.1 M KOH solution. d) Chronoamperometric response obtained for Bat-N-rGO and 19.8% Pt/C catalysts with the addition of methanol after 300 s at rotation speed of 1600 rpm in O_2 saturated solution with a final methanol concentration of 3 M.

oxygen reduction and evolution with a relatively small potential gap (ΔE) of 0.812 V between these two reactions. A 20-hour stability test towards ORR showed that Bat-N-rGO catalyst has a remarkable long-term stability, with only an 8.4% reduction in recorded current over the investigated time-period (Fig. 5c). Furthermore, the SLIB leached residue-based catalyst also exhibited excellent tolerance against methanol poisoning as a mere 16.3% drop in relative current within a 3 M methanol solution was detected – a level that is 2.6 times less than that found for the commercial Pt-based catalyst (Fig. 5d). This demonstrates that Bat-N-rGO catalyst provides outstanding long-term electrocatalytic performance for oxygen reduction, which considerably exceeds the stability of the commercial 19.8% Pt/C catalyst investigated. Various research groups have demonstrated that the carbon doping with cobalt oxides will increase the catalytic performance and stability of ORR and OER [58,62]. Additionally, based on the Rotating Ring Disk Electrode (RRDE) measurements, it was ascertained that Bat-N-rGO catalyst produces H_2O_2 during the oxygen reduction (Fig. S13a), a fact that correlates with previous findings in the literature that carbon based catalysts are excellent peroxide producers in alkaline media [63]. From the results it could be calculated that the number of electrons involved in ORR varies between 3.3 and 3.6 over the disk potential range of 0.7 V to − 0.14 V (Fig. S13b), which indicates that as the applied potential is lowered, the contribution of the four-electron reaction pathway of oxygen reduction increases [64]. The Tafel plots for ORR of Bat-N-rGO exhibit a more moderate slope of − 49 mV dec^{-1} at low overpotentials than that for 19.8% Pt/C − 62 mV dec^{-1}, which signifies that a smaller driving force is required with Bat-N-rGO catalyst for the oxygen reduction process (Fig. S14a). Comparison of Tafel slope values, 49 mV dec^{-1} for Bat-N-rGO and 54 mv dec^{-1} for Bat-rGO over a similar potential range, further shows that the reaction mechanism and rate limiting step differ after the incorporation of nitrogen species and the presence of Co-N-C active sites enhances the ORR activity. In the case of OER, the Bat-N-rGO catalyst had a slope of 75 mV dec^{-1}, which was slightly lower than for the RuO_2 benchmark 79 mV dec^{-1} (Fig. S14b).

3.6. Performance of Bat-N-rGO in Zn-air battery

Beyond the traditional ORR and OER studies, the Bat-N-rGO bifunctional electrocatalyst was also studied in a Zn-air battery (ZAB, Fig. S15) setup as the air cathode catalyst. For comparison, a similar ZAB was assembled, containing state of the art commercial catalyst mixture of Pt/C+RuO_2. Both batteries demonstrated very similar open circuit potential values of 1.50 V for Bat-N-rGO and 1.53 V for Pt/C+RuO_2 catalyst-based systems (Fig. 6a). The battery with Bat-N-rGO catalyst delivered a maximum power density of 112.8 mW cm^{-2} at a current density of 173.5 mA cm^{-2}, which is noticeably higher than what was achieved with the commercial Pt/C+RuO_2 catalyst in the same setup (Fig. 6b, Table S5). Bat-N-rGO demonstrated comparable or even higher maximum power density than what has been reported previously in literature for ZABs with precisely engineered nitrogen and noble metal-free carbon-based bi-functional electrocatalysts by other research groups (Table S5).

At lover current densities, the Bat-N-rGO based system exhibited a somewhat larger charging voltage and therefore, larger voltage gap, between charging and discharging compared to the commercial catalyst mixture (Fig. 6c), this was not unexpected based on RDE results for OER. Additionally, a high specific capacity of 719 mA h g^{-1} was achieved with Bat-N-rGO catalyst, while Pt/C+RuO_2 has 698 mA h g^{-1} at a discharge current of 25 mA cm^{-2} (Fig. 6d). The rechargeability and cycling stability for both catalysts based ZABs were measured at a current density of 5 mA cm^{-2} (Fig. 6e). The galvanostatic cycling tests show that the Bat-N-rGO based ZAB (Fig. 6f) can operate stably over 66 h (400 cycles). The very good structural and morphological stability of the Bat-N-rGO catalyst in the ZAB configuration was also demonstrated based on the SEM images of unused and cycled catalyst layer on the DGL (Fig. S16), where the uniform graphene-like structure is retained even after 60 h of cycling. The ZAB with Pt/C+RuO_2 initially delivers charge and discharge potential over a smaller potential gap, compared to Bat-N-rGO, however this is sustained only up to 40 h, after which the stable performance is quickly lost.
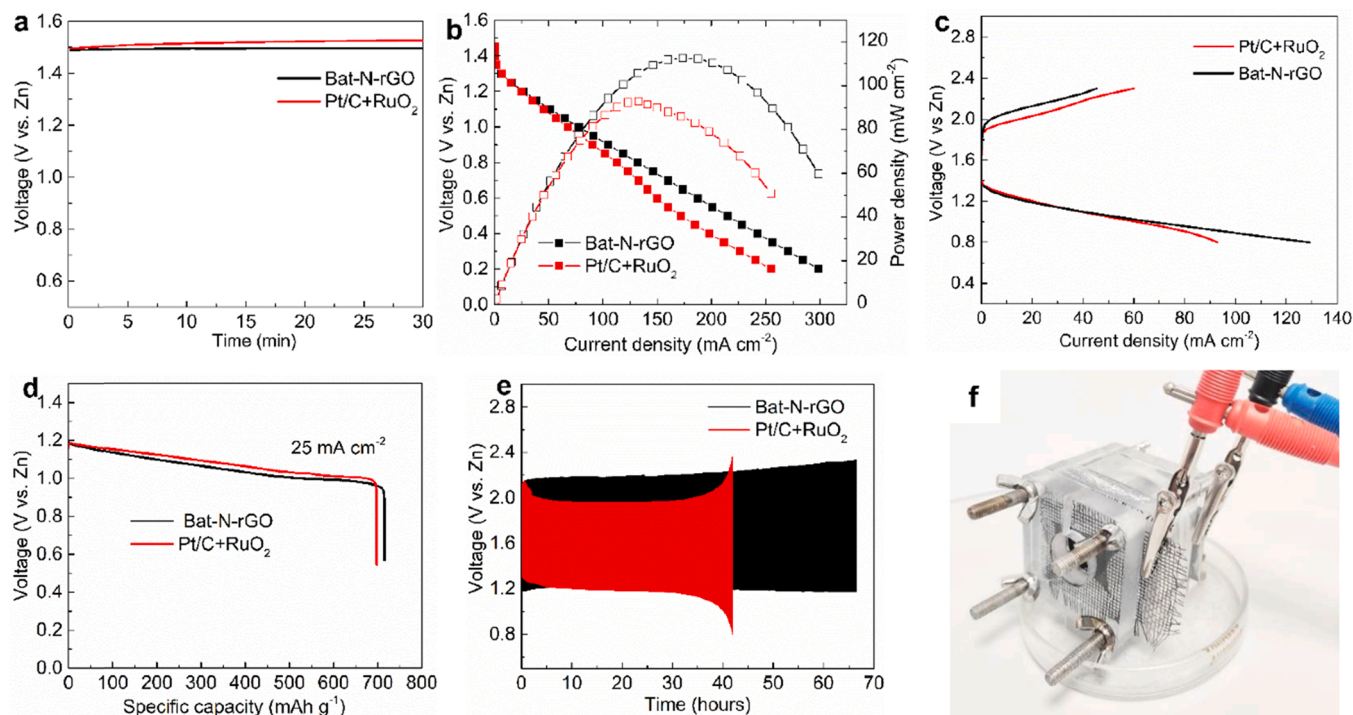

Fig. 6. a) Open circuit plots for Zn-air battery with different air cathode catalysts (Bat-N-rGO and Pt/C+RuO_2). b) discharge polarization curves and the corresponding power density curves, c) charge and discharge polarization curves, d) complete discharge performance of ZAB with Bat-N-rGO and Pt/C+RuO_2 cathode catalyst at 25 mA cm^{-2}, e) galvanostatic discharge/charge cycling of ZAB based on Bat-N-rGO and Pt/C+RuO2 at 5 mA cm^{-2}, f) photograph of a Zn-air battery.

The RDE and measured Zn-air battery results clearly indicate that graphite rich post-metallurgical battery recycling waste fraction can potentially be valorized as a promising source of secondary raw material for catalyst production, thereby further enhancing the materials circularity possible from SLIB wastes. Based on the experimental results above, the bifunctional oxygen electroactivity of Bat-N-rGO catalyst can be attributed to several distinct factors: (1) the presence of a high level of defects and disorder within the carbon structure, which provides the required anchoring sites for cobalt and nitrogen; (2) the existence within the material of inherent Co nanoparticles (1.0 at%) on the surface of catalyst, Co-O-C and Co-C bond accelerating the diffusion of charge; (3) high N-doping (9.8%) level, that was predominated by pyridinic-N species (57%), which increases the number of active sites at the surface of catalyst material and changes the electronic structure, promoting the adsorption of O_2 and intermediates; (4) the co-doping of graphene-like material by nitrogen and cobalt, which promotes the chemical adsorption of oxygen and weakens the O_2 bond; (5) the presence of bamboo-structured carbon nanotubes, that act as a spacers, preventing the restacking of graphene sheets, hence providing a surface with enhanced mass transfer characteristics within the electrode layer.

4. Conclusion

Currently during industrial hydrometallurgical Li-ion battery recycling the spent graphite that remains in the waste is not recovered or valorized. We have developed a new strategy to utilize LIBs black-mass recycling residue as a valuable raw material to produce a bifunctional oxygen electrocatalyst that can be applied in Zn-air batteries and fuel cells. Spent graphite in the post-metallurgical waste residue was turned into valuable graphene-like material, which was spontaneously doped by cobalt due to the traces of cathode metals present remaining in the battery leaching waste after the hydrometallurgical recycling treatment. The Bat-N-rGO electrocatalyst, prepared from this industrial waste, not only exhibited a very high ORR activity, comparable with a 19.8% Pt/C commercial benchmark catalyst, but also an advantageous OER activity, similar to RuO_2 catalyst. Moreover, the Bat-N-rGO bifunctional oxygen electrocatalyst was used in a rechargeable Zn-air battery as an air cathode catalyst and achieved a high-power density of 112.8 mW cm^{-2} and specific capacity 719 mA h g^{-1}, whilst maintaining a good cycling stability. This research for the first time, clearly demonstrates the significant potential of spent Li-ion battery black mass residue as a resource for the more sustainable production of high performance and high value graphene-like catalyst materials for the next-generation electrochemical energy storage and conversion devices required to mitigate climate change.

CRediT authorship contribution statement

K. L. – Conceptualization, Funding acquisition, Investigation, Project administration, Writing – original & reviewed draft. **J. S.** – Investigation (XPS), Writing – original & reviewed draft. **B. P. W.** - Writing – original & reviewed draft. **I. K.** – Resources, Supervision, Writing – original & reviewed draft. **M. L.** – Resources, Supervision, Writing – original & reviewed draft.

Declaration of Competing Interest

The authors declare that they have no known competing financial interests or personal relationships that could have appeared to influence the work reported in this paper.

Data Availability

Data will be made available on request.

Appendix A. Supporting information

Supplementary data associated with this article can be found in the online version at doi:10.1016/j.apcatb.2023.122767.

References

[1] International Energy Agency, Global EV Outlook 2018, 2018. ⟨https://doi.org/10.1787/9789264302365-en⟩.

[2] International Energy Agency, Global EV Outlook 2021 Overview, 2021. ⟨https://www.iea.org/reports/global-ev-outlook-2021⟩.

[3] H.E. Melin, The lithium-ion battery life cycle report 2021, 2021. ⟨https://www.google.com/url?sa=t&rct=j&q=&esrc=s&source=web&cd=&ved=2ahUKEwj6sNWF5cf3AhXKyaQKHSo9AeoQFnoECAcQAQ&url=https%3A%2F%2Fstatic1.squarespace.com%2Fstatic%2F587657ddbe659497fb46664c%2Ft%2F5fdaa991dc2ddb6396c30fa6%2F1608165783527%2FThe%2Blithium-ion⟩.

[4] P. Kauranen, I.V. Kojo, O. Salmi, A. Vassart, M. Lundström, S. Sayfritz, E. Wiesner, V. Trapp, F. Forte, V. Faucheux, M. Zygmunt, W. Tomboy, J.-L. Bazin, F. Hilario, K. Päivi, B. Pereira, C. Pettit, C. Van der Eijk, P. Roschger, C. Berruti, N. Gonzales Ramon, J.M. Míguez, M. Philippot, C. Capiglia, A. Witomski, E. Hakanen, A. Ibañez, Y. Le Petit, Batteries Europe ETIP WG2: Raw Materials and Recycling Roadmap, 2021. ⟨https://ec.europa.eu/energy/content/batteries-europe-raw-materials-and-recycling-roadmap_en⟩.

[5] M. Rinne, H. Elomaa, A. Porvali, M. Lundström, Simulation-based life cycle assessment for hydrometallurgical recycling of mixed LIB and NiMH waste, Resour. Conserv. Recycl. 170 (2021), 105586, https://doi.org/10.1016/j.resconrec.2021.105586.

[6] D.L. Thompson, J.M. Hartley, S.M. Lambert, M. Shiref, G.D.J. Harper, E. Kendrick, P. Anderson, K.S. Ryder, L. Gaines, A.P. Abbott, The importance of design in lithium ion battery recycling-a critical review, Green Chem. 22 (2020) 7585–7603, https://doi.org/10.1039/d0gc02745f.

[7] Y. Wang, N. An, L. Wen, L. Wang, X. Jiang, F. Hou, Y. Yin, J. Liang, Recent progress on the recycling technology of Li-ion batteries, J. Energy Chem. 55 (2020) 391–419, https://doi.org/10.1016/j.jechem.2020.05.008.

[8] L. Brückner, J. Frank, T. Elwert, Industrial recycling of lithium-ion batteries—A critical review of metallurgical process routes, Metals 10 (2020) 1–29, https://doi.org/10.3390/met10081107.

[9] M.T. Islam, U. Iyer-Raniga, Lithium-ion battery recycling in the circular economy: a review, Recycling 7 (2022) 1–40, https://doi.org/10.3390/recycling7030033.

[10] European commision, Regulation of the European Parliament and of the Council concerning batteries and waste batteries, repealing. Directive 2006/66/EC and amending Regulation (EU) No 2019/1020, 2020. ⟨https://eur-lex.europa.eu/legal-content/EN/TXT/?uri=CELEX%3A52020PC0798⟩.

[11] European Commission, Critical Raw Materials Resilience: Charting a Path towards greater Security and Sustainability, 2020. ⟨http://info.worldbank.org/governance/wgi/⟩.

[12] European Commission, Study on the EU's list of Critical Raw Materials (2020), 2020. ⟨https://doi.org/10.2873/92480⟩.

[13] S. Windisch-Kern, E. Gerold, T. Nigl, A. Jandric, M. Altendorfer, B. Rutrecht, S. Scherhaufer, H. Raupenstrauch, R. Pomberger, H. Antrekowitsch, F. Part, Recycling chains for lithium-ion batteries: A critical examination of current challenges, opportunities and process dependencies, Waste Manag 138 (2022) 125–139, https://doi.org/10.1016/j.wasman.2021.11.038.

[14] H. Ali, H.A. Khan, M. Pecht, Preprocessing of spent lithium-ion batteries for recycling: Need, methods, and trends, Renew. Sustain. Energy Rev. 168 (2022), 112809, https://doi.org/10.1016/j.rser.2022.112809.

[15] R. Golmohammadzadeh, F. Faraji, B. Jong, C. Pozo-Gonzalo, P.C. Banerjee, Current challenges and future opportunities toward recycling of spent lithium-ion batteries, Renew. Sustain. Energy Rev. 159 (2022), 112202, https://doi.org/10.1016/j.rser.2022.112202.

[16] D. Latini, M. Vaccari, M. Lagnoni, M. Orefice, F. Mathieux, J. Huisman, L. Tognotti, A. Bertei, A comprehensive review and classification of unit operations with assessment of outputs quality in lithium-ion battery recycling, J. Power Sources 546 (2022), 231979, https://doi.org/10.1016/j.jpowsour.2022.231979.

[17] A. Porvali, A. Chernyaev, S. Shukla, M. Lundström, Lithium ion battery active material dissolution kinetics in Fe(II)/Fe(III) catalyzed Cu-H2SO4 leaching system, Sep. Purif. Technol. 236 (2020), 116305, https://doi.org/10.1016/j.seppur.2019.116305.

[18] A. Chernyaev, J. Partinen, L. Klemettinen, B.P. Wilson, A. Jokilaakso, M. Lundström, The efficiency of scrap Cu and Al current collector materials as

reductants in LIB waste leaching, Hydrometallurgy 203 (2021) 1–10, https://doi.org/10.1016/j.hydromet.2021.105608.

[19] J. Liu, H. Shi, X. Hu, Y. Geng, L. Yang, P. Shao, X. Luo, Critical strategies for recycling process of graphite from spent lithium-ion batteries: A review, Sci. Total Environ. 816 (2022), 151621, https://doi.org/10.1016/j.scitotenv.2021.151621.

[20] S. Natarajan, V. Aravindan, An urgent call to spent LIB recycling: whys and wherefores for graphite recovery, Adv. Energy Mater. 10 (2020) 1–8, https://doi.org/10.1002/aenm.202002238.

[21] A. Vanderbruggen, J. Sygusch, M. Rudolph, R. Serna-Guerrero, A contribution to understanding the flotation behavior of lithium metal oxides and spheroidized graphite for lithium-ion battery recycling, Coll. Surf. A Physicochem. Eng. Asp. 626 (2021), 127111, https://doi.org/10.1016/j.colsurfa.2021.127111.

[22] A. Vanderbruggen, A. Salces, A. Ferreira, M. Rudolph, R. Serna-Guerrero, Improving separation efficiency in end-of-life lithium-ion batteries flotation using attrition pre-treatment, Minerals 12 (2022) 72, https://doi.org/10.3390/min12010072.

[23] A. Dańczak, R. Ruismäki, T. Rinne, L. Klemettinen, H. O'brien, P. Taskinen, A. Jokilaakso, R. Serna-Guerrero, Worth from waste: Utilizing a graphite-rich fraction from spent lithium-ion batteries as alternative reductant in nickel slag cleaning, Minerals 11 (2021) 784, https://doi.org/10.3390/min11070784.

[24] R. Ruismäki, T. Rinne, A. Danczak, P. Taskinen, R. Serna-Guerrero, A. Jokilaakso, Integrating flotation and pyrometallurgy for recovering graphite and valuable metals from battery scrap, Metals 10 (2020) 1–22.

[25] W. Zhang, Z. Liu, J. Xia, F. Li, W. He, G. Li, J. Huang, Preparing graphene from anode graphite of spent lithium-ion batteries, Front. Environ. Sci. Eng. 11 (2017) 1–8, https://doi.org/10.1007/s11783-017-0993-8.

[26] L. Wang, L. Yang, G. Xu, Q. Peng, Y. Li, E. Zhao, J. Ma, S. Fan, X. Li, Separation and recovery of carbon powder in anodes from spent lithium-ion batteries to synthesize graphene, Sci. Rep. 9 (2019) 9823, https://doi.org/10.1038/s41598-019-46393-4.

[27] L. Ye, C. Wang, L. Cao, H. Xiao, J. Zhang, B. Zhang, X. Ou, Effective regeneration of high-performance anode material recycled from the whole electrodes in spent lithium-ion batteries via a simplified approach, Green Energy Environ. 6 (2021) 725–733, https://doi.org/10.1016/j.gee.2020.06.017.

[28] S. Natarajan, S. Rao Ede, H.C. Bajaj, S. Kundu, Environmental benign synthesis of reduced graphene oxide (rGO) from spent lithium-ion batteries (LIBs) graphite and its application in supercapacitor, Coll. Surf. A Physicochem. Eng. Asp. 543 (2018) 98–108, https://doi.org/10.1016/j.colsurfa.2018.01.054.

[29] J.S. Ribeiro, M.B.J.G. Freitas, J.C.C. Freitas, Recycling of graphite and metals from spent Li-ion batteries aiming the production of graphene/CoO-based electrochemical sensors, J. Environ. Chem. Eng. 9 (2021), 104689, https://doi.org/10.1016/j.jece.2020.104689.

[30] K. Liivand, M. Kazemi, P. Walke, V. Mikli, M. Uibu, D. Macdonald, I. Kruusenberg, Spent Li-ion battery graphite turned into valuable and active catalyst for electrochemical oxygen reduction, ChemSusChem 14 (2021) 1103–1111, https://doi.org/10.1002/cssc.202002742.

[31] X. Zhu, J. Xiao, Q. Mao, Z. Zhang, Z. You, L. Tang, Q. Zhong, A promising regeneration of waste carbon residue from spent Lithium-ion batteries via low-temperature fluorination roasting and water leaching, Chem. Eng. J. 430 (2022), 132703, https://doi.org/10.1016/j.cej.2021.132703.

[32] P.G. Schiavi, P. Altimari, R. Zanoni, F. Pagnanelli, Full recycling of spent lithium ion batteries with production of core-shell nanowires//exfoliated graphite asymmetric supercapacitor, J. Energy Chem. 58 (2021) 336–344, https://doi.org/10.1016/j.jechem.2020.10.025.

[33] H.F. Wang, C. Tang, Q. Zhang, A review of precious-metal-free bifunctional oxygen electrocatalysts: rational design and applications in Zn−air batteries, Adv. Funct. Mater. 28 (2018) 1803329, https://doi.org/10.1002/adfm.201803329.

[34] S. Ren, X. Duan, S. Liang, M. Zhang, H. Zheng, Bifunctional electrocatalysts for Zn-air batteries: Recent developments and future perspectives, J. Mater. Chem. A 8 (2020) 6144–6182, https://doi.org/10.1039/c9ta14231b.

[35] H. Wang, J. Chen, Y. Lin, X. Wang, J. Li, Y. Li, L. Gao, L. Zhang, D. Chao, X. Xiao, J. M. Lee, Electronic modulation of non-van der waals 2D electrocatalysts for efficient energy conversion, Adv. Mater. 33 (2021) 1–25, https://doi.org/10.1002/adma.202008422.

[36] X. Wu, C. Tang, Y. Cheng, X. Min, S.P. Jiang, S. Wang, Bifunctional catalysts for reversible oxygen evolution reaction and oxygen reduction reaction, Chem. A Eur. J. 26 (2020) 3906–3929, https://doi.org/10.1002/chem.201905346.

[37] H. Wang, J. Li, K. Li, Y. Lin, J. Chen, L. Gao, V. Nicolosi, X. Xiao, J.M. Lee, Transition metal nitrides for electrochemical energy applications, Chem. Soc. Rev. 50 (2021) 1354–1390, https://doi.org/10.1039/d0cs00415d.

[38] V. Jose, J.M.V. Nsanzimana, H. Hu, J. Choi, X. Wang, J.M. Lee, Highly efficient oxygen reduction reaction activity of N-doped carbon–cobalt boride heterointerfaces, Adv. Energy Mater. 11 (2021) 1–9, https://doi.org/10.1002/aenm.202010157.

[39] P. Serp, B. Machado, Carbon (Nano)materials for Catalysis, in: Nanostructured Carbon Mater. Catal., 2015: pp. 1–45. https://doi.org/https://doi.org/10.1039/9781782622567.

[40] M.S. Ahmed, B. Choi, Y.B. Kim, Development of highly active bifunctional electrocatalyst using coon carbon nanotubes for oxygen reduction and oxygen evolution, Sci. Rep 8 (2018) 2543, https://doi.org/10.1038/s41598-018-20974-1.

[41] I. Kruusenberg, D. Ramani, S. Ratso, U. Joost, R. Saar, P. Rauwel, A.M. Kannan, K. Tammeveski, Cobalt–nitrogen Co-doped carbon nanotube cathode catalyst for alkaline membrane fuel cells, ChemElectroChem 3 (2016) 1455–1465, https://doi.org/10.1002/celc.201600241.

[42] K.M. Villemson, K. Kaare, R. Raudsepp, T. Käämbre, K.N. Šmits, P. Wang, A. V. Kuzmin, A. Šutka, B.A. Shainyan, I. Kruusenberg, Identification of active sites for

oxygen reduction reaction on nitrogen- and sulfur-codoped carbon catalysts, J. Phys. Chem. C 123 (2019) 16065–16074, https://doi.org/10.1021/acs.jpcc.9b00117.

[43] V. Jose, H. Hu, E. Edison, W. Manalastas, H. Ren, P. Kidkhunthod, S. Sreejith, A. Jayakumar, J.M.V. Nsanzimana, M. Srinivasan, J. Choi, J.M. Lee, Modulation of single atomic Co and Fe sites on hollow carbon nanospheres as oxygen electrodes for rechargeable Zn–Air batteries, Small Methods 5 (2021) 1–10, https://doi.org/10.1002/smtd.202000751.

[44] W.S. Hummers, R.E. Offeman, Preparation of graphitic oxide, J. Am. Chem. Soc. 80 (1958) 1339, https://doi.org/10.1021/ja01539a017.

[45] S. Ratso, I. Kruusenberg, M. Vikkisk, U. Joost, E. Shulga, I. Kink, T. Kallio, K. Tammeveski, Highly active nitrogen-doped few-layer graphene/carbon nanotube composite electrocatalyst for oxygen reduction reaction in alkaline media, Carbon N. Y 73 (2014) 361–370, https://doi.org/10.1016/j.carbon.2014.02.076.

[46] J. Pudas, A. Erkkila, J. Viljamaa, Battery recycling method, WO2011113860A1, 2011.

[47] A. Porvali, M. Aaltonen, S. Ojanen, O. Velazquez-martinez, E. Eronen, F. Liu, B. P. Wilson, R. Serna-guerrero, M. Lundström, Resources, Conservation & Recycling Mechanical and hydrometallurgical processes in HCl media for the recycling of valuable metals from Li-ion battery waste, Resour. Conserv. Recycl. 142 (2019) 257–266, https://doi.org/10.1016/j.resconrec.2018.11.023.

[48] A. Vanderbruggen, E. Gugala, R. Blannin, K. Bachmann, R. Serna-Guerrero, M. Rudolph, Automated mineralogy as a novel approach for the compositional and textural characterization of spent lithium-ion batteries, Miner. Eng. 169 (2021), 106924, https://doi.org/10.1016/j.mineng.2021.106924.

[49] S. Wang, S. Chen, L. Ma, J.A. Zapien, Recent progress in cobalt-based carbon materials as oxygen electrocatalysts for zinc-air battery applications, Mater. Today Energy 20 (2021), 100659, https://doi.org/10.1016/j.mtener.2021.100659.

[50] A.E. Lewis, Review of metal sulphide precipitation, Hydrometallurgy 104 (2010) 222–234, https://doi.org/10.1016/j.hydromet.2010.06.010.

[51] H. Estay, L. Barros, E. Troncoso, Metal sulfide precipitation: recent breakthroughs and future outlooks, Minerals 11 (2021) 1385, https://doi.org/10.3390/min11121385.

[52] Z. Jia, K. Kou, M. Qin, H. Wu, F. Puleo, L.F. Liotta, Controllable and large-scale synthesis of carbon nanostructures: A review on bamboo-like Nanotubes, Catalysts 7 (2017), https://doi.org/10.3390/catal7090256.

[53] L.S. Lobo, S.A.C. Carabineiro, Explaining bamboo-like carbon fiber growth mechanism: catalyst shape adjustments above tammann temperature, C. J. Carbon Res. 6 (2020) 18, https://doi.org/10.3390/c6020018.

[54] A. Ashok, A. Kumar, J. Ponraj, S.A. Mansour, Synthesis and growth mechanism of bamboo like N-doped CNT/Graphene nanostructure incorporated with hybrid metal nanoparticles for overall water splitting, Carbon N. Y 170 (2020) 452–463, https://doi.org/10.1016/j.carbon.2020.08.047.

[55] S. Chen, J. Bi, Y. Zhao, L. Yang, C. Zhang, Y. Ma, Q. Wu, X. Wang, Z. Hu, Nitrogen-doped carbon nanocages as efficient metal-free electrocatalysts for oxygen reduction reaction, Adv. Mater. 24 (2012) 5593–5597, https://doi.org/10.1002/adma.201202424.

[56] Z. Huang, Z. Liao, W. Yang, H. Zhou, C. Fu, Y. Gong, L. Chen, Y. Kuang, Different types of nitrogen species in nitrogen-doped carbon material: The formation mechanism and catalytic role on oxygen reduction reaction, Electrochim. Acta 245 (2017) 957–966, https://doi.org/10.1016/j.electacta.2017.06.063.

[57] C. Tang, B. Wang, H.F. Wang, Q. Zhang, Defect engineering toward atomic Co–Nx–C in hierarchical graphene for rechargeable flexible solid Zn-air batteries, Adv. Mater. 29 (2017) 1–7, https://doi.org/10.1002/adma.201703185.

[58] M.C. Biesinger, B.P. Payne, A.P. Grosvenor, L.W.M. Lau, A.R. Gerson, R.S.C. Smart, Resolving surface chemical states in XPS analysis of first row transition metals, oxides and hydroxides: Cr, Mn, Fe, Co and Ni, Appl. Surf. Sci. 257 (2011) 2717–2730, https://doi.org/10.1016/j.apsusc.2010.10.051.

[59] T. Zhang, C. He, F. Sun, Y. Ding, M. Wang, L. Peng, J. Wang, Y. Lin, Co3O4 nanoparticles anchored on nitrogen-doped reduced graphene oxide as a multifunctional catalyst for H2O2 reduction, oxygen reduction and evolution reaction, Sci. Rep. 7 (2017) 1–11, https://doi.org/10.1038/srep43638.

[60] C. Mao, M. Wood, L. David, S.J. An, Y. Sheng, Z. Du, H.M. Meyer, R.E. Ruther, D. L. Wood, Selecting the best graphite for long-life, high-energy Li-ion batteries, J. Electrochem. Soc. 165 (2018) A1837–A1845, https://doi.org/10.1149/2.1111809jes.

[61] J. Chang, Y. Wang, L. Chen, D. Wu, F. Xu, Z. Bai, K. Jiang, Z. Gao, Cobalt nanoparticles embedded nitrogen doped carbon, preparation from alkali deprotonation assisted ZIF-67 and its electrocatalytic performance in oxygen evolution reaction, Int. J. Hydrog. Energy 45 (2020) 12787–12797, https://doi.org/10.1016/j.ijhydene.2020.02.206.

[62] Y.X. Zhao, X. Guo, X. Zhai, Y.M. Yan, K.N. Sun, Diethylenetriamine (DETA)-assisted anchoring of Co3O4 nanorods on carbon nanotubes as efficient electrocatalysts for the oxygen evolution reaction, J. Mater. Chem. A 3 (2015) 1761–1768, https://doi.org/10.1039/c4ta04641b.

[63] G. Zhang, Q. Wei, X. Yang, A.C. Tavares, S. Sun, RRDE experiments on noble-metal and noble-metal-free catalysts: Impact of loading on the activity and selectivity of oxygen reduction reaction in alkaline solution, Appl. Catal. B Environ. 206 (2017) 115–126, https://doi.org/10.1016/j.apcatb.2017.01.001.

[64] A. Kostuch, J. Gryboś, S. Wierzbicki, Z. Sojka, K. Kruczała, Selectivity of mixed iron-cobalt spinels deposited on a n,s-doped mesoporous carbon support in the oxygen reduction reaction in alkaline media, Materials 14 (2021) 1–19, https://doi.org/10.3390/ma14040820.